Simultaneous Hyperpolarized ^{13}C-Pyruvate MRI and ^{18}F-FDG PET (HyperPET) in 10 Dogs with Cancer

Henrik Gutte[1], Adam E. Hansen[1], Majbrit M.E. Larsen[2], Sofie Rahbek[1], Sarah T. Henriksen[1,3], Helle H. Johannesen[1], Jan Ardenkjaer-Larsen[3,4], Annemarie T. Kristensen[2], Liselotte Højgaard[1], and Andreas Kjær[1]

[1]Department of Clinical Physiology, Nuclear Medicine & PET and Cluster for Molecular Imaging, Rigshospitalet, University of Copenhagen, Copenhagen, Denmark; [2]Department of Veterinary Clinical and Animal Sciences, Faculty of Health and Medical Sciences, University of Copenhagen, Frederiksberg C, Denmark; [3]Department of Electrical Engineering, Technical University of Denmark, Lyngby, Denmark; and [4]GE Healthcare, Brøndby, Denmark

With the introduction of combined PET/MR spectroscopic (MRS) imaging, it is now possible to directly and indirectly image the Warburg effect with hyperpolarized ^{13}C-pyruvate and ^{18}F-FDG PET imaging, respectively, via a technique we have named hyperPET. The main purpose of this present study was to establish a practical workflow for performing ^{18}F-FDG PET and hyperpolarized ^{13}C-pyruvate MRS imaging simultaneously for tumor tissue characterization and on a larger scale test its feasibility. In addition, we evaluated the correlation between ^{18}F-FDG uptake and ^{13}C-lactate production. **Methods:** Ten dogs with biopsy-verified spontaneous malignant tumors were included for imaging. All dogs underwent a protocol of simultaneous ^{18}F-FDG PET, anatomic MR, and hyperpolarized dynamic nuclear polarization with ^{13}C-pyruvate imaging. The data were acquired using a combined clinical PET/MR imaging scanner. **Results:** We found that combined ^{18}F-FDG PET and ^{13}C-pyruvate MRS imaging was possible in a single session of approximately 2 h. A continuous workflow was obtained with the injection of ^{18}F-FDG when the dogs was placed in the PET/MR scanner. ^{13}C-MRS dynamic acquisition demonstrated in an axial slab increased ^{13}C-lactate production in 9 of 10 dogs. For the 9 dogs, the ^{13}C-lactate was detected after a mean of 25 s (range, 17–33 s), with a mean to peak of ^{13}C-lactate at 49 s (range, 40–62 s). ^{13}C-pyruvate could be detected on average after 13 s (range, 5–26 s) and peaked on average after 25 s (range, 13–42 s). We noticed concordance of ^{18}F-FDG uptake and production of ^{13}C-lactate in most, but not all, axial slices. **Conclusion:** In this study, we have shown in a series of dogs with cancer that hyperPET can easily be performed within 2 h. We showed mostly correspondence between ^{13}C-lactate production and ^{18}F-FDG uptake and expect the combined modalities to reveal additional metabolic information to improve prognostic value and improve response monitoring.

Key Words: cancer; dynamic nuclear polarization; hyperpolarized; ^{13}C-pyruvate; MR; ^{18}F-FDG PET; PET/MR; molecular imaging

As established almost a century ago, cancer cell metabolism differs from normal cells. A central metabolic characteristic in malignant cancer cells is the shift to glycolysis with production of lactate even in the presence of sufficient oxygen (aerobic glucolysis) (*1–4*), a phenomenon first described by Heinrich Otto Warburg in 1924 (*5,6*) and later named the Warburg effect. In normal nonhypoxic cells, glucose utilization by oxidative phosphorylation is considerably more efficient in ATP (adenosine triphosphate) production. Therefore, even when cancer cells do not have a higher energy need, 10- to 20-fold-higher amounts of glucose are consumed in these cells than in normal cells (*7*). This leads to excessive uptake of glucose, which is the foundation for visualization of malignant tumors using the glucose analog ^{18}F-FDG (*8,9*) with PET (*1,3*).

Anatomic imaging with CT often in combination with ^{18}F-FDG PET is currently the method of choice in the response evaluation of cancer therapy in patients, although the value of CT is limited because of great variation in anatomic response to treatment (*10*). A more sensitive and reliable method for noninvasive in vivo imaging of early treatment response and thereby also in drug development is therefore warranted. MR spectroscopy (MRS) is a potent technique for noninvasive in vivo investigation of tissue chemistry and cellular metabolism (*11*). Dynamic nuclear polarization is capable of creating solutions of molecules with polarized nuclear spins in different nuclei, and it is now possible to do real-time investigation of in vivo metabolism. The development of this technique has increased the nuclear polarization more than 10,000-fold, thus significantly increasing the sensitivity of MRS (*12,13*). Additionally, the technique allows measurement of the kinetics of the conversion of metabolites and can be combined with proton MR imaging. Various nuclei have been hyperpolarized using the dynamic nuclear polarization technique (*14,15*). Currently, the most widely used nucleus is ^{13}C because of the possibility of incorporating ^{13}C into relevant compounds. Depending on the tissue, disease, and metabolic state investigated, intravenous injection of hyperpolarized ^{13}C-pyruvate results in an increase of ^{13}C-lactate, ^{13}C-alanine, and ^{13}CO$_2$ resonance peaks (*12,16*). In particular, direct imaging of the Warburg effect in tumors is possible based on ^{13}C-pyruvate to ^{13}C-lactate conversion (*16–19*).

With the introduction of combined PET/MR imaging, it is now possible to directly and indirectly image the Warburg effect with hyperpolarized ^{13}C-pyruvate and ^{18}F-FDG PET in a single imaging session as recently shown by us in 1 dog. We named this combined technique hyperPET (*20*).

With the present study, we aimed at moving from proof of concept in a single dog to establishing a practical workflow and demonstrating the feasibility of hyperPET on a larger scale using a series of 10 dogs with cancer. In addition, we evaluated the correlation between ^{18}F-FDG uptake and ^{13}C-lactate production.

MATERIALS AND METHODS

Study Population

Ten dogs with biopsy-verified spontaneous malignant tumors were included for imaging as part of staging of their tumor. The dog characteristics are given in Table 1. Before hyperPET, the dogs underwent routine staging procedures for their particular tumor except evaluation for distant disease, which was performed as part of the hyperPET protocol.

All dogs underwent a protocol of simultaneous ^{18}F-FDG PET, anatomic MR, and hyperpolarized dynamic nuclear polarization ^{13}C-pyruvate spectroscopic imaging. The data were acquired using a combined clinical PET/MR imaging scanner (mMR Biograph; Siemens). In all cases, hyperpolarized ^{13}C-pyruvate MRS was performed on the primary tumor. Depending on tumor size, 1–3 slabs were studied (Table 2).

The dogs were premedicated with methadone (0.2 mg/kg intramuscularly), anesthetized using a bolus injection of propofol, and maintained by a continuous intravenous infusion of propofol (15–25 mg/kg/h) or by administration of an air/oxygen-enriched gas mixture with sevoflurane. Heart rate, oxygen saturation, and blood pressure were measured throughout the scanning procedure. MR imaging was performed using a ^{1}H/^{13}C dual tuned flex coil (RAPID Biomedical). For MR flip angle calibration and frequency centering, a 5.5-mL vial of 4.0 M ^{13}C-urea mixed with gadolinium (Dotarem; Guerbet) was placed at the back of the coil. The coil was placed as close as possible to the tumor and centered on the lesion.

The Ethics and Administrative Committee, Department of Veterinary Clinical and Animal Sciences, Faculty of Health and Medical Sciences, University of Copenhagen, approved the study.

Hyperpolarized ^{13}C-Pyruvate Preparation

Hyperpolarized ^{13}C-pyruvate was obtained with a SpinLab (GE Healthcare) using the dynamic nuclear polarization technique. [1-^{13}C]pyruvic acid was mixed with an electron paramagnetic agent (PN AH111501; Syncom). The electron paramagnetic agent concentration in the sample was 15 mM. The dissolution medium consisted of ethylenediaminetetraacetic acid disodium salt dehydrate (0.1 g/L)

(PN E4994; Sigma) in water. Before injection, the hyperpolarized ^{13}C-pyruvate was neutralized with 0.72 M NaOH, 0.4 M Tris, and ethylenediaminetetraacetic acid disodium salt (0.1 g/L) in water. The amount injected was 0.68 mL/kg of body weight.

[1]H MR Imaging

Localizer images and manual ^{13}C flip angle calibration were followed by anatomic ^{1}H MR imaging, including T2 turbo spin-echo (TSE) (repetition time [TR], 4,000 ms; echo time [TE], 89 ms; voxel size, 0.6×0.5 mm^2; 19 slices of 3-mm thickness) in 3 planes and transverse T1 TSE (TR, 550 ms; TE, 6.5 ms; voxel size, 0.7×0.6 mm^2; 27 slices of 3-mm thickness). Finally, after acquisition of chemical shift imaging (CSI) and ^{18}F-FDG PET, a transverse fat-saturated T1 TSE with the same parameters as the first T1 TSE was performed after gadolinium injection (0.1 mL/kg [Gadovist]) in most dogs.

^{18}F-FDG PET Imaging

PET was performed as a single-bed, 4- to 10-min acquisition, with intravenous injection of 8 MBq/kg of ^{18}F-FDG. The duration for PET imaging was determined by the maximal approved time of anesthesia of 2 h as stated by the Ethical and Administrative committee, University of Copenhagen. Images were reconstructed using 3-dimensional ordinary Poisson ordered-subset expectation maximization (3D-OP-OSEM), with 4 iterations, 21 subsets, a matrix size of 344×344, 4-mm gaussian postprocessing filter, and vendor-supplied attenuation-correction algorithms. The pixel size for PET imaging datasets was 2.1×2.1 mm with a 2.03-mm slice thickness.

Dynamic ^{13}C-MRS

In an axially/oblique-oriented 40-mm-thick slab including the tumor region, dynamic ^{13}C-MRS was performed (TR, 1,000 ms; TE, 0.757 ms; flip angle, 5°; bandwidth, 4,000 Hz). The acquisition was repeated for a total duration of 3 min starting at the injection of the hyperpolarized ^{13}C-pyruvate.

[13]C CSI

For ^{13}C metabolic imaging, 2-dimensional CSI was used. [13]C CSI was acquired just after ^{18}F-FDG PET and 30–50 s after injection of hyperpolarized ^{13}C-pyruvate (TR, 80 ms; flip angle, 10°; bandwidth, 10,000 Hz; field of view, 80–120 mm; slice thickness, 13–23 mm; matrix, 16×16 [circular truncation]; and total imaging time, 11 s). The field of view was adjusted according to the organ of interest. The 30- to 50-s delay was chosen to obtain maximum ^{13}C-lactate signal during CSI based on the previous dynamic ^{13}C-MRS acquisition. When possible within the maximal approved total anesthesia time of 2 h, the

TABLE 1
Characteristics of the Dogs

Dog	Tumor	Tumor localization	Weight (kg)
1	Liposarcoma	Right forepaw	32
2	Carcinoma	Thyroid	50
3	Sarcoma	Subcutaneous, between eye and nose	15
4	Sarcoma	Left back paw	42
5	Sarcoma	Nasal cavity	40
6	Sarcoma	Nasal cavity	13
7	Fibrosarcoma	Right maxilla	50
8	Sarcoma	Right tonsil	23
9	Chondrosarcoma	Nasal cavity	29
10	Osteosarcoma	Back	18

TABLE 2
Characteristic for All CSI Slices Obtained with Corresponding Standardized Uptake Values, Tumor Size, and CSI Voxel Size

Dog	Slice no.	CSI slice location	Tumor size (diameter [cm])	SUV_{mean}	SUV_{max}	SUV_{min}	CSI voxel size (mm)	^{13}C-lactate, r	^{13}C-pyruvate/ ^{13}C-lactate, r
1	1	Axial slice of primary tumor	2.3	0.9	1.4	0.2	5	0.32*	0.69[†]
3	1	Axial slice of primary tumor	2.1	2.7	4.2	1.2	5	0.45[†]	0.74[†]
	2	Sagittal slice of primary tumor	2.6	2.9	4.3	1.6	5	0.7	0.83[†]
4	1	Axial slice of primary tumor	5.2	1.9	3.7	0.5	7.5	0.28*	0.62[†]
	2	Coronal slice of primary tumor	5.6	2.2	4	0.7	5	0.22	0.53[†]
5	1	Axial slice of primary tumor	1.9	6.6	9.2	3	5	0.55[†]	0.48[†]
6	1	Axial slice of primary tumor	2.3	2.4	3.3	1.4	5	0.58	[‡]
7	1	Axial slice of primary tumor	4.9	2.4	3.5	0.5	7.5	0.78[†]	−0.24
	2	Axial slice of primary tumor	4.1	2.4	3.7	1.2	7.5	0.62*	0.24
8	1	Axial slice of primary tumor	2.2	2.8	4.3	1.2	7.5	0.66[†]	0.48
	2	Axial slice of lymph node	3.6	2.4	3.3	1.1	7.5	0.67	−0.81
9	1	Axial slice of primary tumor	2.5	1.5	2.2	0.9	6.3	0.43*	−0.42*
	2	Axial slice of primary tumor	2.4	1.7	2.7	1	6.3	0.82[†]	0.83[†]
10	1	Axial slice of primary tumor	6	1.4	2.9	0.2	10	0.50[†]	−0.30*
	2	Axial slice of primary tumor	5.6	1.4	2.7	0.5	10	0.75[†]	−0.26
	3	Axial slice of primary tumor	5.7	1.3	2.4	0.3	10	0.79[†]	0.41

*$P < 0.05$.
[†]$P < 0.001$.
[‡]Only 2 voxels in corresponding CSI; therefore, it was not possible to calculate correlation.
SUV_{mean}, SUV_{max}, and SUV_{min} = mean, maximum, and minimum standardized uptake values, respectively.
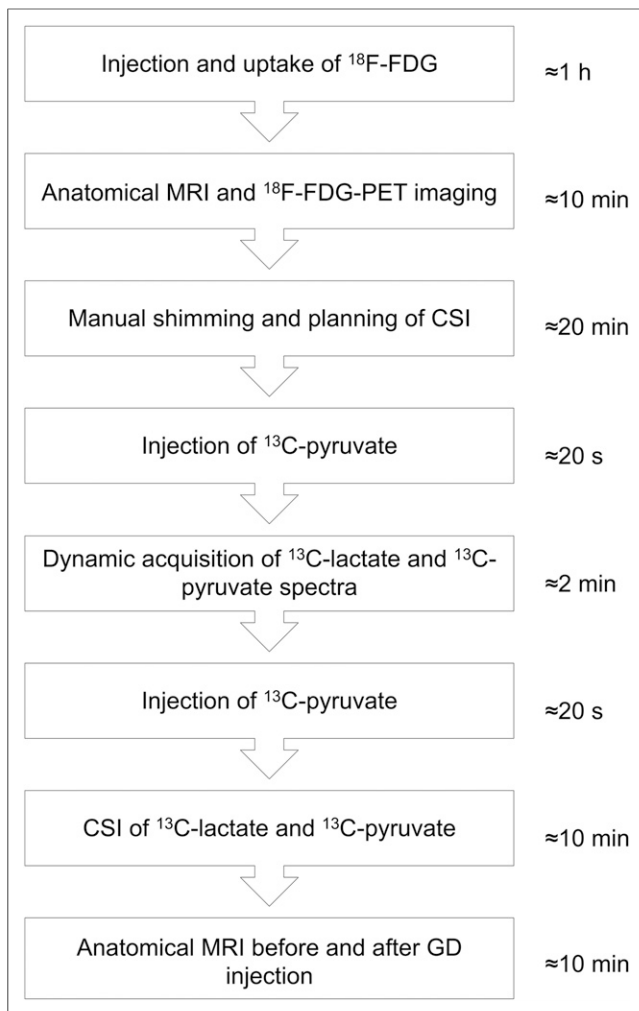Slabs of tumor are through lesion at different levels. Table shows maximum SUV correlation (r) with corresponding P values for ^{13}C-lactate and ratio of ^{13}C-pyruvate to ^{13}C-lactate.

CSI was repeated in different parts of the tumor or in metastatic regions. The number of slabs for each tumor is given in Table 2. Peak heights of [1-^{13}C]-pyruvate, [1-^{13}C]-lactate, [1-^{13}C]-alanine, and [1-^{13}C]-pyruvate hydrate were quantified using a general linear model implemented in Matlab (The MathWorks) and applied in the time domain. We reported the magnitude of peak heights resulting from the modeling. When reporting a metabolite ratio, the normalization was performed to the sum of all modeled peak heights.

Postprocessing of ^{13}C CSI and ^{18}F-FDG PET

All ^{13}C CSI datasets were converted to DICOM format. The ^{18}F-FDG PET, ^{1}H MR imaging, and ^{13}C MRS datasets were visualized and analyzed using the open source OsiriX imaging software (version

5.9; PIXMEO). All datasets were automatically fused. CSI voxels with a modeled ^{13}C-lactate and ^{13}C-pyruvate peak height above a threshold of 4 times the SD of noise in a silent region of the spectrum were used in the correlation matrix for each individual dog. The regions of interest derived were hence superimposed and applied to the CSI datasets of ^{13}C-lactate, ^{13}C-pyruvate, and ^{18}F-FDG PET. ^{18}F-FDG uptake was calculated and reported as standardized uptake values according to the following formula: (measured activity concentration [MBq/mL] × body weight [g]/injected activity [MBq]) × 1,000 (g/kg). Mean, minimum, and maximum uptake values of ^{18}F-FDG were determined. Values obtained from the ^{13}C MR metabolite images were expressed in arbitrary units.

FIGURE 1. Workflow of hyperPET acquisition. GD = gadolinium.

Acquisition of dynamic ^{13}C-lactate and ^{13}C-pyruvate spectra lasted less than 10 min. ^{13}C-lactate and ^{13}C-pyruvate CSI was repeated 2–3 times and lasted approximately 10 min. Finally a T1 TSE sequence before and after gadolinium injection was performed that lasted less than 10 min.

^{13}C MRS Dynamic Acquisition

^{13}C MRS dynamic acquisition demonstrated in the axial slab an increased ^{13}C-lactate production in 9 of 10 dogs. For dog 6, no ^{13}C signal was observed in the dynamic spectra because of an erroneous calibration of the flip angle.
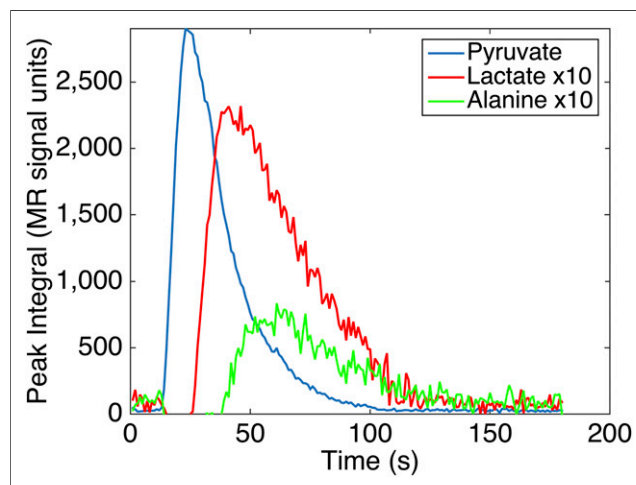
The dynamic acquisition provided spectra from the axial slab (with a time resolution of 1 s) that covered the tumor region and surrounding tissues. These dynamic data showed reproducible uptake of hyperpolarized ^{13}C-pyruvate in the tumor and the conversion to hyperpolarized ^{13}C-lactate as demonstrated in Figure 2 (dog 8). In this dog, during dynamic acquisition ^{13}C-pyruvate was seen 20 s after the injection of the ^{13}C-pyruvate bolus, with a peak at 24 s. ^{13}C-lactate appeared after 25 s and reached a maximum about 40 s after injection of the ^{13}C-pyruvate bolus.

For the 9 dogs, the ^{13}C-lactate was seen initially after a mean of 25 s (range, 17–33 s), with a mean peak of ^{13}C-lactate after 49 s (range, 40–62 s), whereas the ^{13}C-pyruvate initially was seen after a mean of 13 s (range, 5–26 s), with peak after a mean of 25 s (range, 13–42 s) (Table 3).

^{13}C MRS Imaging and ^{18}F-FDG PET

The metabolite images (Figs. 3 and 4; Supplemental Fig. 1; supplemental materials are available at http://jnm.snmjournals. org) are a result of an interpolation of the 16 × 16 voxels. In the ^{13}C-lactate/^{13}C-pyruvate image, voxels with a ratio based on signal in the level of pure noise have been removed from the interpolated overlays.

We noticed voxel-by-voxel concordance of ^{18}F-FDG uptake and production of ^{13}C-lactate in most axial slabs. This is illustrated

A voxel-per-voxel correlation analysis was performed comparing the ^{18}F-FDG PET and ^{13}C CSI datasets. Each slice consisted of 16 × 16 voxels of 5.0 × 5.0 to 10.0 × 10.0 mm. All statistical analyses were performed in SPSS Statistics (version 22; IBM). A *P* value of less than 0.05 was considered significant. For time analysis, dynamic ^{13}C-MRS curves were noise-filtered with a gaussian having a full width at half maximum of 1.5 s.

RESULTS

HyperPET Workflow

We found that combined ^{18}F-FDG PET and ^{13}C-pyruvate MRS imaging was possible in a single session of approximately 2 h. A continuous workflow was obtained with injection of ^{18}F-FDG after the dog was placed in the PET/MR scanner. An outline of the workflow is shown in Figure 1.

Positioning of the coil, induction of anesthesia, positioning of the dog, and PET/MR imaging planning were achieved initially and lasted approximately 1 h. After approximately 60 min, an ^{18}F-FDG PET/MR scan lasting 4–10 min was acquired. ^{1}H MR imaging and ^{18}F-FDG PET acquisition were performed simultaneously. Manual shimming and planning of the CSI took approximately 20 min and was immediately followed by dissolution and injection of ^{13}C-pyruvate that took less than 30 s in our setup.

FIGURE 2. Typical graph of dynamic acquisition from axial slab through sarcoma in tonsil (dog 8). Graphs are generated from a slab through single lesion biopsy–verified tumor and of nonmalignant tissue. ^{13}C-pyruvate was seen 20 s after injection of ^{13}C-pyruvate bolus and peaked at 24 s. ^{13}C-lactate appeared after 25 s and reached maximum about 40 s after injection of ^{13}C-pyruvate bolus.

TABLE 3
Time to Peak, Time to Initiate, and Ratio Peak Values of ^{13}C-Lactate and ^{13}C-Pyruvate for All Dogs

Dog	^{13}C-pyruvate time to peak (s)	^{13}C-lactate delay (s)	^{13}C-lactate time to peak (s)	^{13}C-lactate time to initiate (s)	^{13}C-lactate % of peak at 50 s
1	21	29	50	28	100
2	21	21	42	17	93
3	13	34	47	21	92
4	25	16	41	21	94
5	42	20	62	28	73
7	30	20	50	28	100
8	24	16	40	27	94
9	25	37	62	33	83
10	21	30	51	22	100
Mean (range)	25 (13–42)	25 (16–37)	49 (40–62)	25 (17–33)	92 (73–100)

Values were generated from dynamic acquisition from axial slab including single lesion biopsy–verified tumor.

in dog 4 (Fig. 3), in whom a heterogeneous uptake of ^{18}F-FDG PET in a sarcoma located on the hind limb partly corresponded to ^{13}C-lactacte production (Fig. 3). Additionally, we found a voxel-by-voxel association between maximum uptake of ^{18}F-FDG and the ratio of ^{13}C-lactate to ^{13}C-pyruvate ($r = 0.62$, $P < 0.0001$) in the same axial slab as illustrated in Figure 5.

In dog 7, we were able to demonstrate a more homogeneous uptake of ^{18}F-FDG in a fibrosarcoma located intramuscularly in the neck (Supplemental Fig. 1). This uptake strongly correlated with the production of ^{13}C-lactate as illustrated in the scatterplot in Supplemental Figure 2 ($r = 0.78$; $P < 0.0001$). In dog 8 with tonsil cancer and a lymph node metastasis, we demonstrated an increased ^{13}C-lactate production in the metastasized lymph node. We found that the ^{13}C-lactate production and the CSI ^{13}C-lactate–to–^{13}C-pyruvate ratio matched the uptake of ^{18}F-FDG, and it was possible to visualize the central necrotic core of the lymph node as also demonstrated in the anatomic MR imaging sequence. There was loss of ^{13}C signal in the profound part of the neck and tumor due to the profile of the dual tuned surface coil.
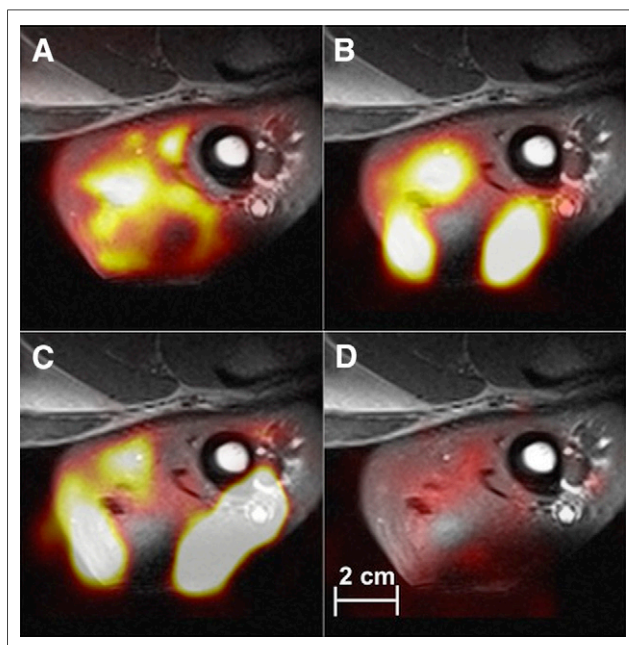
FIGURE 3. Axial slab of sarcoma located on hind leg (dog 4, slice 1). Imaging of ^{18}F-FDG PET/MR (A), CSI of ^{13}C-lactate (B), ^{13}C-pyruvate (C), and ratio of ^{13}C-lactate to ^{13}C-pyruvate (D) demonstrate heterogeneous uptake of ^{18}F-FDG, which partly corresponds to ^{13}C-lactacte production. CSI and ^{18}F-FDG PET pixel sizes are 7.5 × 7.5 and 2.1 × 2.1 mm, respectively.
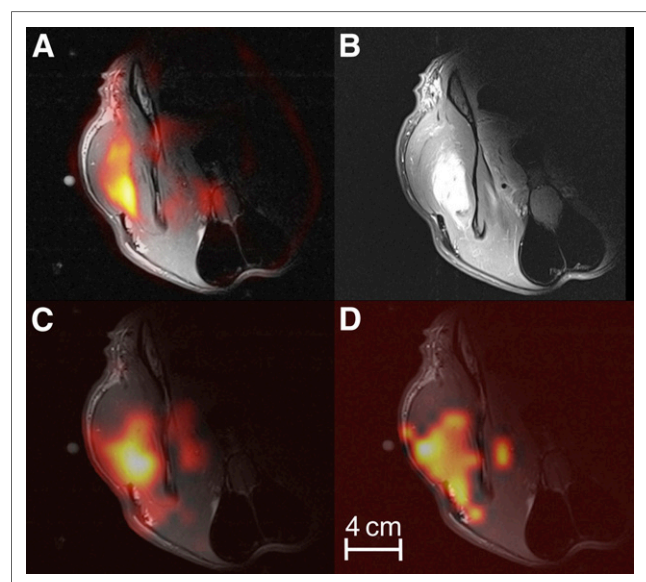
FIGURE 4. Axial slice of dog 7 (slice 1), demonstrating relatively homogeneous uptake of ^{18}F-FDG (A: ^{18}F-FDG PET/MR) in intramuscular fibrosarcoma located in neck. Corresponding gadolinium uptake in tumor as demonstrated in T1 (TSE) image can be seen in B. Also ^{13}C-lactate (C) and ratio of ^{13}C-lactate to ^{13}C-pyruvate (D) were relatively homogeneously distributed. CSI and ^{18}F-FDG PET pixel sizes are 7.5 × 7.5 and 2.1 × 2.1 mm, respectively.
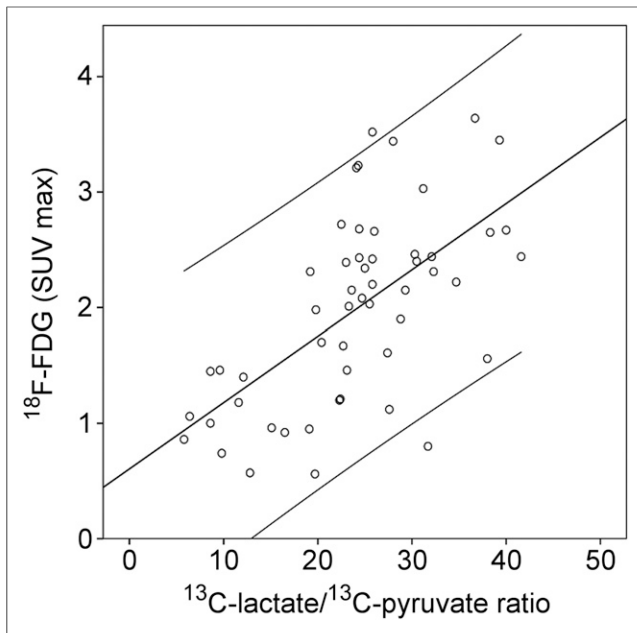
FIGURE 5. Scatterplot showing significant correlation of maximum uptake of ^{18}F-FDG and ratio of ^{13}C-lactate to ^{13}C-pyruvate in 16 × 16 voxels (size, 7.5 × 7.5 mm) in single slice of sarcoma (dog 4, axial slice 1). Lines are 95% individual prediction intervals. $r = 0.62$; $P < 0.0001$. SUV = standardized uptake value.

DISCUSSION

To our knowledge, this is the first study acquiring both ^{13}C-lactate/^{13}C-pyruvate CSI and ^{18}F-FDG PET imaging in consecutive spontaneous malignant tumors using a combined clinical PET/MR scanner. We were able, with a workflow of approximately 2 h, to visualize in real time the in vivo metabolism of ^{13}C-pyruvate and its conversion into ^{13}C-lactate in 9 consecutive dogs. This study therefore demonstrates that tumor imaging with hyperPET is feasible for dogs with biopsy-verified spontaneous tumors.

Rather than using mice with human xenograph tumors, we used naturally developing malignant cancers in dogs as a model for human disease. Cancer-bearing dogs represent a unique clinical cancer model with a direct potential for accelerating translation into human patients (*21*). This is because companion dogs with spontaneous cancer resemble the heterogeneity in human cancers, with similarity of metastasis, local invasion, tumor stromal interaction, and resistance to therapy. Therefore, the current study also indicates that our new workflow will be feasible in human cancer patients. As an added benefit, the information gained by PET/MR supported dog management including prognostication and therapy planning for each of the dogs.

We have in this study demonstrated that ^{18}F-FDG uptake and ^{13}C-lactate production were somewhat concordant in most of the assessed cancers. However, we also showed that ^{18}F-FDG uptake and ^{13}C-lactate differ in some cases, which underlines the different processes visualized by the 2 modalities and the potential added value of combining the methods. Whereas increased glucose uptake (^{18}F-FDG) is a compound measure of several hallmarks of cancer (*22*), for example, cell proliferation, hypoxia, and metabolic changes, measured ^{13}C-pyruvate to ^{13}C-lactate conversion probably demonstrates the Warburg effect per se. Prostate, neuroendocrine, and cerebral tumors are potential

cancer forms that might benefit from hyperPET using PET tracers other than ^{18}F-FDG, thereby obtaining a more detailed characterization of cancer in a 1-stop-shop scan. The better characterization can be used for personalizing therapy and evaluation of treatment response.

The relatively large voxel size of CSI compared with ^{18}F-FDG PET allowed only for rough correlation analyses.

From a practical viewpoint, hyperPET may seem unrealistic to perform as a clinical routine. However, we were able to perform hyperPET within a 2-h time slot. This workflow even included a ^{13}C-pyruvate injection and dynamic acquisition to establish the time point for the following high-resolution CSI. Variations in time–concentration curves are probably due to differences in cardiovascular status, size of animal, perfusion of tumor, and malignancy grade of the tumor. The acquisitions can currently not be performed in a single session. Accordingly, in our study we evaluated the variation in the peak of ^{13}C-lactate to see whether a fixed time point would be possible to use. The peak was observed between 40 and 62 s (average, 49 s) after ^{13}C-pyruvate injection, possibly indicating that a fixed time point of approximately 50 s could be used, which could remove the necessity of performing an individual dynamic scan. If 50 s had been used, 7 of 9 dogs had a ^{13}C-lactate level above 90% of peak (Table 3). This is a minor deviation, and therefore we suggest that use of a fixed time point is feasible. Using a fixed time point will save both time and 1 production of hyperpolarized ^{13}C-pyruvate per dog, simplifying the workflow even more.

Ideally, more advanced MR imaging sequences will allow for faster, volumetric and repeated spectroscopic imaging (*23,24*). Such MR imaging sequences consequently permit for larger spatial resolution and additional detailed characterization of the tumor metabolism. However, newer sequences, which are able to demonstrate the dynamics of the metabolism, are aimed to be
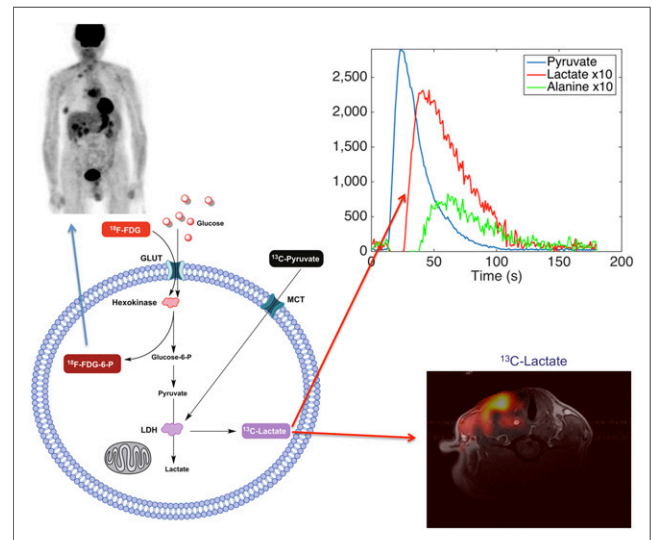
FIGURE 6. Concept of hyperPET and characterization of Warburg effect. Whereas increased ^{18}F-FDG uptake is compound measure of several hallmarks of cancer, for example, cell proliferation, hypoxia, and metabolic changes, measured ^{13}C-pyruvate to ^{13}C-lactate conversion probably demonstrates the Warburg effect per se. GLUT = glucose transporters; LDH = lactate dehydrogenase; MCT = monocarboxylate transporters. Modified from Gutte et al. (*20*).

developed and to be used in future studies. Until then we support a fixed time point based on pilot studies.

Another challenge of CSI is loss of signal. In an approximately 5-cm depth, 50% of the signal is lost due to the coil profile of the surface coil used in this study. However, most of the tumors investigated were located at or close to the surface of the animal, and therefore we were able to gain sufficient signal. However, other coils, for example, body coils, need to be applied if larger and more profound tumors are to be evaluated.

Recently, a first-in-human 31-patient study was conducted with the primary objective to assess the safety of hyperpolarized ^{13}C-pyruvate in healthy subjects and prostate cancer patients. The study showed an elevated ^{13}C-lactate–to–^{13}C-pyruvate ratio in regions of biopsy-proven prostate cancer (*19*). However, so far the technique has never been combined with PET in humans.

Only preclinical comparisons have been performed and that being on separate PET and MR systems (*25,26*), with potential errors arising from the time difference between the examinations and the repositioning of the animal. Admittedly, it may not be with ^{18}F-FDG that the time difference is the largest challenge but with other potential PET tracers to be combined with CSI. The introduction of integrated clinical PET/MR systems allows for single-session, simultaneous MR imaging and PET.

HyperPET first described by us and now performed in a series of 10 dogs with cancer may soon be translated into human patients. Whether the combined modalities are better than CSI or PET alone remains to be proven. However, the different processes visualized indicate that better prognostic value and early response monitoring may be obtained. An outline of the concept of hyperPET imaging is presented in Figure 6.

CONCLUSION

In this study, we have shown in a series of dogs with cancer that hyperPET can easily be performed within 2 h. We showed some but not total correspondence between ^{13}C-lactate production and ^{18}F-FDG uptake, indicating that the compound measure may carry additional information for better prognostication, tumor characterization, and response monitoring in cancer.

DISCLOSURE

ACKNOWLEDGMENTS

REFERENCES

1. Johnbeck CB, Jensen MM, Nielsen CH, Hag AMF, Knigge U, Kjær A. ^{18}F-FDG and ^{18}F-FLT-PET imaging for monitoring everolimus effect on tumor-growth in neuroendocrine tumors: studies in human tumor xenografts in mice. *PLoS One.* 2014;9:e91387.
2. Vander Heiden MG, Cantley LC, Thompson CB. Understanding the Warburg effect: the metabolic requirements of cell proliferation. *Science.* 2009;324:1029–1033.
3. Jensen MM, Erichsen KD, Johnbeck CB, et al. [^{18}F]FDG and [^{18}F]FLT positron emission tomography imaging following treatment with belinostat in human ovary cancer xenografts in mice. *BMC Cancer.* 2013;13:168.
4. Bartrons R, Caro J. Hypoxia, glucose metabolism and the Warburg's effect. *J Bioenerg Biomembr.* 2007;39:223–229.
5. Warburg O. On the origin of cancer cells. *Science.* 1956;123:309–314.
6. Cairns RA, Harris IS, Mak TW. Regulation of cancer cell metabolism. *Nat Rev Cancer.* 2011;11:85–95.
7. Gatenby RA, Gillies RJ. Why do cancers have high aerobic glycolysis? *Nat Rev Cancer.* 2004;4:891–899.
8. Kjær A, Loft A, Law I, et al. PET/MRI in cancer patients: first experiences and vision from Copenhagen. *MAGMA.* 2013;26:37–47.
9. Hansen AE, Kristensen AT, Jørgensen JT, et al. ^{64}Cu-ATSM and ^{18}FDG PET uptake and ^{64}Cu-ATSM autoradiography in spontaneous canine tumors: comparison with pimonidazole hypoxia immunohistochemistry. *Radiat Oncol.* 2012;7:89.
10. Wahl RL, Jacene H, Kasamon Y, Lodge MA. From RECIST to PERCIST: evolving considerations for pet response criteria in solid tumors. *J Nucl Med.* 2009;50:122S–150S.
11. Shah N, Sattar A, Benanti M, Hollander S, Cheuck L. Magnetic resonance spectroscopy as an imaging tool for cancer: a review of the literature. *J Am Osteopath Assoc.* 2006;106:23–27.
12. Ardenkjaer-Larsen JH, Fridlund B, Gram A, et al. Increase in signal-to-noise ratio of > 10,000 times in liquid-state NMR. *Proc Natl Acad Sci USA.* 2003;100:10158–10163.
13. Ardenkjaer-Larsen JH, Leach AM, Clarke N, Urbahn J, Anderson D, Skloss TW. Dynamic nuclear polarization polarizer for sterile use intent. *NMR Biomed.* 2011;24:927–932.
14. Gallagher FA, Kettunen MI, Day SE, et al. Detection of tumor glutamate metabolism in vivo using ^{13}C magnetic resonance spectroscopy and hyperpolarized [1-^{13}C]glutamate. *Magn Reson Med.* 2011;66:18–23.
15. Gallagher FA, Kettunen MI, Brindle KM. Imaging pH with hyperpolarized ^{13}C. *NMR Biomed.* 2011;24:1006–1015.
16. Brindle KM, Bohndiek SE, Gallagher FA, Kettunen MI. Tumor imaging using hyperpolarized ^{13}C magnetic resonance spectroscopy. *Magn Reson Med.* 2011;66:505–519.
17. Golman K, Zandt RIT, Lerche MH, Pehrson R, Ardenkjaer-Larsen JH. Metabolic imaging by hyperpolarized 13c magnetic resonance imaging for in vivo tumor diagnosis. *Cancer Res.* 2006;66:10855–10860.
18. Albers MJ, Bok RA, Chen AP, et al. Hyperpolarized ^{13}C lactate, pyruvate, and alanine: noninvasive biomarkers for prostate cancer detection and grading. *Cancer Res.* 2008;68:8607–8615.
19. Nelson SJ, Kurhanewicz J, Vigneron DB, et al. Metabolic imaging of patients with prostate cancer using hyperpolarized [1-^{13}C]pyruvate. *Sci Transl Med.* 2013;5:198ra108.
20. Gutte H, Hansen AE, Henriksen ST, et al. Simultaneous hyperpolarized ^{13}C-pyruvate MRI and ^{18}F-FDG-PET in cancer (hyperPET): feasibility of a new imaging concept using a clinical PET/MRI scanner. *Am J Nucl Med Mol Imaging.* 2015;5:38–45.
21. Hansen AE, Kristensen AT, Law I, McEvoy FJ, Kjær A, Engelholm SA. Multimodality functional imaging of spontaneous canine tumors using 64 Cu-ATSM and 18 FDG PET/CT and dynamic contrast enhanced perfusion CT. *Radiother Oncol.* 2012;102:424–428.
22. Hanahan D, Weinberg RA. Hallmarks of cancer: the next generation. *Cell.* 2011;144:646–674.
23. Hurd RE, Yen Y-FF, Chen AP, Ardenkjaer-Larsen JH. Hyperpolarized ^{13}C metabolic imaging using dissolution dynamic nuclear polarization. *J Magn Reson Imaging.* 2012;36:1314–1328.
24. Nelson SJ, Ozhinsky E, Li Y, Park I, Crane J. Strategies for rapid in vivo ^{1}H and hyperpolarized ^{13}C MR spectroscopic imaging. *J Magn Reson.* 2013;229:187–197.
25. Witney TH, Kettunen MI, Day SE, et al. A comparison between radiolabeled fluorodeoxyglucose uptake and hyperpolarized ^{13}C-labeled pyruvate utilization as methods for detecting tumor response to treatment. *Neoplasia.* 2009;11:574–582.
26. Menzel MI, Farrell EV, Janich MA, et al. Multimodal Assessment of in vivo metabolism with hyperpolarized [1-^{13}C]MR spectroscopy and ^{18}F-FDG PET imaging in hepatocellular carcinoma tumor-bearing rats. *J Nucl Med.* 2013;54:1113–1119.